

# Journal of Biomedical Optics

[SPIDigitalLibrary.org/jbo](http://SPIDigitalLibrary.org/jbo)

## **Spectrally resolving and scattering-compensated x-ray luminescence/fluorescence computed tomography**

Wenxiang Cong  
Haiou Shen  
Ge Wang

# Spectrally resolving and scattering-compensated x-ray luminescence/fluorescence computed tomography

Wenxiang Cong, Haiou Shen, and Ge Wang

Virginia Polytechnic Institute and State University, School of Biomedical Engineering and Sciences, Biomedical Imaging Division, Blacksburg, Virginia 24061

**Abstract.** The nanophosphors, or other similar materials, emit near-infrared (NIR) light upon x-ray excitation. They were designed as optical probes for *in vivo* visualization and analysis of molecular and cellular targets, pathways, and responses. Based on the previous work on x-ray fluorescence computed tomography (XFCT) and x-ray luminescence computed tomography (XLCT), here we propose a spectrally-resolving and scattering-compensated x-ray luminescence/fluorescence computed tomography (SXLCT or SXFCT) approach to quantify a spatial distribution of nanophosphors (other similar materials or chemical elements) within a biological object. In this paper, the x-ray scattering is taken into account in the reconstruction algorithm. The NIR scattering is described in the diffusion approximation model. Then, x-ray excitations are applied with different spectra, and NIR signals are measured in a spectrally resolving fashion. Finally, a linear relationship is established between the nanophosphor distribution and measured NIR data using the finite element method and inverted using the compressive sensing technique. The numerical simulation results demonstrate the feasibility and merits of the proposed approach. © 2011 Society of Photo-Optical Instrumentation Engineers (SPIE). [DOI: 10.1117/1.3592499]

Keywords: optical molecular imaging; nanophosphors; x-ray fluorescence computed tomography; x-ray luminescence computed tomography; spectrally-resolving; scattering-compensated; image reconstruction; compressive sensing; Bregman iteration.

Paper 10644RR received Dec. 7, 2010; revised manuscript received Apr. 15, 2011; accepted for publication Apr. 28, 2011; published online Jun. 13, 2011.

## 1 Introduction

Novel contrast agents provide outstanding opportunities to visualize and analyze specific biological targets, signal pathways, and therapeutic responses.<sup>1,2</sup> The nanophosphors, or other similar materials, emit near-infrared (NIR) luminescence light upon x-ray excitation.<sup>3,4</sup> As optical probes, these nanophosphors potentially allow sensitive and specific high-resolution imaging *in vivo*.<sup>5</sup>

Using the nanophosphors, x-ray luminescence computed tomography (XLCT) was recently proposed as a new molecular imaging modality.<sup>6</sup> The experiments demonstrated that XLCT could image the cross-sectional distribution of nanophosphors.<sup>7</sup> XLCT has several advantages compared to other optical molecular imaging modalities. First, the anatomy and the nanophosphors can be imaged in one scan. Second, the use of x-ray excitation eliminates the autofluorescence in optical fluorescence imaging. Third, the straight line propagation of x-rays in a biological object means a localized and deep probing capability, promising to significantly improve the spatial resolution.<sup>6</sup> Through selective excitation with a pencil x-ray beam, XLCT can perform *in vivo* tomographic imaging on a region of interest (ROI) to reduce radiation dose and shorten experimental time.<sup>8–10</sup> This selective excitation mechanism is similar to x-ray fluorescence computed tomography (XFCT), which is used to map elements inside samples.<sup>11</sup> Recently, XFCT is applied for gold nanoparticle imaging at relatively low concentrations using polychromatic diagnostic x-rays.<sup>12</sup>

However, a primary issue with XLCT is related to the x-ray scattering effect. For example, x-ray Compton scattering is the major component in water for energy  $>40$  keV.<sup>13</sup> The XLCT reconstruction will be significantly compromised if the luminescence signal induced by these scattered x-ray photons is not effectively compensated. In this paper, we propose a systematic approach to address the x-ray scattering effects in the XLCT reconstruction. Furthermore, x-ray excitations are preferably applied with different spectra, and NIR signals are measured in a spectrally resolving fashion. Finally, a linear relationship is established between the nanophosphor distribution and the measured NIR data using the finite element method and inverted using the compressive sensing (CS) technique. This methodology can be adapted for x-ray fluorescence computed tomography (XFCT) as well. Hence, our approach is for spectrally-resolving and scattering-compensated x-ray luminescence/fluorescence computed tomography (SXLCT or SXFCT) for significantly better imaging performance.

In Sec. 2, we will first formulate the scattering-compensated XLCT, and then extend it for multi-spectral scattering-compensated XLCT. In Sec. 3, numerical results are reported to demonstrate the feasibility and merits of the proposed approach in each of the aforementioned two cases. In Sec. 4, relevant issues are discussed, and finally the paper is concluded.

## 2 Imaging Model

Nanophosphors can be functionalized, introduced into a biological object such as a mouse, and bound to specific cells or markers in the tissue.<sup>2</sup> When an x-ray beam irradiates the

---

Address all correspondence to: Ge Wang, Virginia Tech, School of Biomedical Engineering and Sciences, Stanger Street, Blacksburg, Virginia 24061; Tel: 540-231-0493; Fax: 540-231-0970; E-mail: wangg@vt.edu.

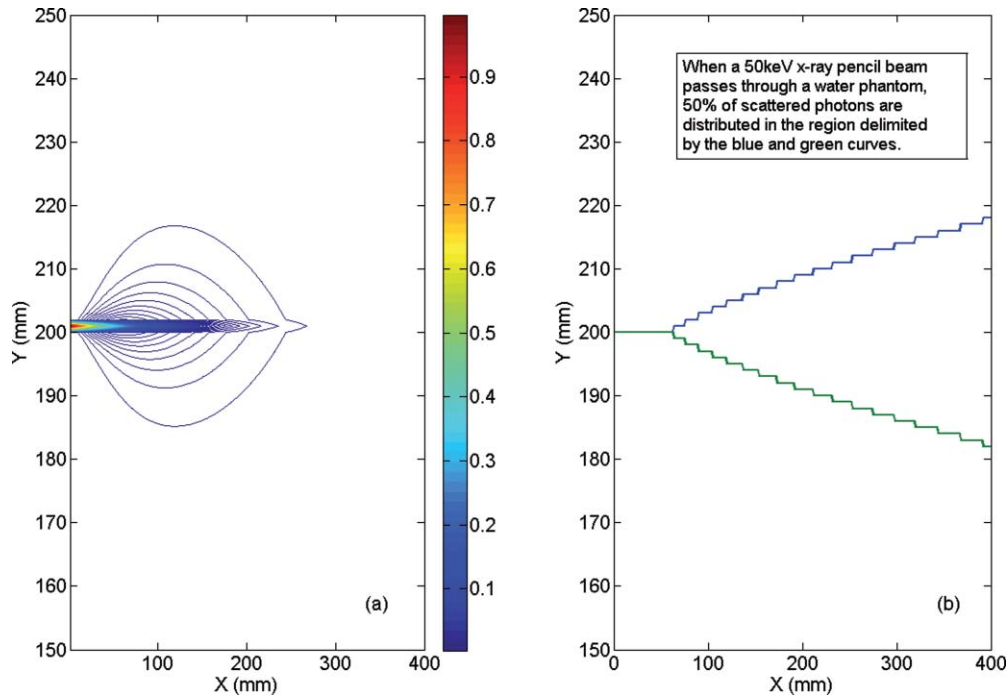


**Fig. 1** Significance of x-ray scattering. (a) X-ray pencil beam passes through a water phantom and (b) 50% of scattered photons are distributed in the region delimited by the blue and green curves.

tissue, the nanophosphors along the x-ray path will be excited to emit NIR light, which can then be captured by an optical sensor. Our SXLCT algorithm is proposed to accurately localize and reliably quantify the nanophosphor distribution in the tissue from the surface NIR measurements and prior knowledge. The algorithm is based on the photon propagation models in the NIR and x-ray energy ranges, respectively.

## 2.1 X-ray Transport

Currently, one often assumes that the x-ray beam is limited in the primary path as in Ref. 6. However, a significant part of the x-ray energy is scattered away from the primary path, and the scattered x-ray photons would induce nanophosphor luminescence outside the primary x-ray path. Hence, the x-ray scattering effect should be included in the x-ray photon transport model. X-ray scattering can be incoherent (Compton scattering) or coherent (Rayleigh scattering).<sup>13,14</sup> While an x-ray beam propagates through a tissue along a straight line, the x-ray intensity distribution  $I(\mathbf{r})$  along the primary path can be computed by the Lambert-Beer formula

$$I(\mathbf{r}) = I_0 \exp \left[ - \int_0^1 \mu_t [(1-\tau) \mathbf{r}_0 + \tau \mathbf{r}] d\tau \right], \quad (1)$$

where  $\mathbf{r}_0$  is a source position,  $I_0$  is the x-ray source intensity, and  $\mu_t$  is the attenuation coefficient that can be computed from measured x-ray transmission data in the XLCT system using an attenuation-based computed tomography (CT) technique. From the definition of the differential cross section of x-ray photon scattering, the x-ray single scattering intensity at a position  $\mathbf{r}$  from the primary x-ray beam can be described as

follows:

$$\begin{aligned} X(\mathbf{r}) = & \int_L I(\mathbf{r}_s) \eta(\mathbf{r}_s) \frac{d\sigma_{scatter}}{d\Omega}(\beta) \\ & \times \exp \left[ - \int_0^1 \mu_t [(1-\tau) \mathbf{r}_s + \tau \mathbf{r}] d\tau \right] d\mathbf{r}_s, \quad (2) \end{aligned}$$

where  $L$  is a line segment as the intersection between the x-ray primary beam and the object,  $\beta$  is the x-ray photon scattering angle computed by  $\beta = \cos^{-1} \left( \frac{(\mathbf{r}-\mathbf{r}_s) \cdot \mathbf{v}}{\|\mathbf{r}-\mathbf{r}_s\|} \right)$ ,  $\mathbf{v}$  is the direction of the x-ray primary beam,  $\eta(\mathbf{r}_s)$  is the electron density at the position  $\mathbf{r}_s$ , and the x-ray differential scattering cross-section  $\frac{d\sigma_{scatter}}{d\Omega}(\beta)$  can be evaluated by the Klein-Nishina formula and the differential cross section of Rayleigh scattering.<sup>14</sup> Quantitatively, we estimated the x-ray scattering effect. A cubic phantom of 40 mm side length was filled with pure water. An x-ray pencil beam of diameter 0.2 mm at 50 keV perpendicularly irradiated the phantom at the center of one surface. The attenuation coefficient and the electron density of water are  $0.214 \text{ (cm}^{-1}\text{)}$  and  $3.346 \times 10^{23} \text{ /cm}^3$ , respectively. The x-ray scattering distribution is shown in Fig. 1. The x-ray scattering effect can be also modeled using a Monte Carlo simulation method,<sup>15</sup> an approximation Monte Carlo technique,<sup>16</sup> a radiative transport equation solver, or its variant to take multiple-scattering photons into account.

## 2.2 Near-infrared Light Transport

NIR light is subject to both scattering and absorption. The biological soft tissue has highly scattering and weakly absorbing properties in the NIR spectral region. In this case, the diffusion approximation (DA) model usually offers an accurate description for NIR light transport<sup>17</sup>

$$-\nabla \cdot [D(\mathbf{r}) \nabla \Phi(\mathbf{r})] + \mu_a(\mathbf{r}) \Phi(\mathbf{r}) = S(\mathbf{r}), \quad \mathbf{r} \in \Omega, \quad (3)$$

where  $\mathbf{r}$  is the position vector,  $\Phi(\mathbf{r})$  is the NIR photon fluence rate,  $S(\mathbf{r})$  is the NIR source,  $\mu_a$  is the absorption coefficient,  $D$  is the diffusion coefficient defined by  $D = [3(\mu_a + \mu'_s)]^{-1}$ ,  $\mu'_s$  is the reduced scattering coefficient, and  $\Omega \subset \mathbb{R}^3$  is a region of interest. If no photon travels across the boundary  $\partial\Omega$  into the tissue domain  $\Omega$ , the DA is constrained by the Robin boundary condition

$$\Phi(\mathbf{r}) + 2\alpha D(\mathbf{r})[\nu \cdot \nabla \Phi(\mathbf{r})] = 0, \quad \mathbf{r} \in \partial\Omega, \quad (4)$$

where  $\nu$  is the outward unit normal vector on  $\partial\Omega$ , and  $\alpha$  is the boundary mismatch factor. The boundary mismatch factor between the tissue with a refractive index  $n$  and air can be approximated by  $\alpha = (1 + \gamma)/(1 - \gamma)$  with  $\gamma = -1.4399n^{-2} + 0.7099n^{-1} + 0.6681 + 0.0636n$ .<sup>17</sup> The measurable exiting photon flux on the surface of the object can be expressed as

$$m(\mathbf{r}) = -D(\mathbf{r})(\nu \cdot \nabla \Phi(\mathbf{r})) \quad \mathbf{r} \in \partial\Omega. \quad (5)$$

The intensity of the emitted NIR light depends on the nanophosphor density  $\rho(\mathbf{r})$ , the x-ray intensity  $X(\mathbf{r})$ , and the light yield  $\varepsilon$ , which can be defined as the quantum yield per unit nanophosphor concentration. The light yield can be experimentally determined. Although that dependency is nonlinear, in this feasibility study we assume that the intensity of NIR light is linearly proportional to both the x-ray dose and nanophosphor concentration,<sup>5</sup>

$$S(\mathbf{r}) = \varepsilon X(\mathbf{r}) \rho(\mathbf{r}). \quad (6)$$

Note that the luminescence phenomenon may also depend on the energy of the incoming x-ray beam but is temporarily ignored for simplicity.

### 2.3 Discretization

Equations (3) and (4) can be discretized into a matrix equation linking the nanophosphor distribution  $\rho$  and the NIR photon fluence rate  $\Phi(\mathbf{r})$  at a node  $\mathbf{r}$  using the finite element analysis,<sup>18</sup>

$$\mathbf{A} \cdot \Phi = \mathbf{F} \cdot \rho, \quad (7)$$

where the component of the matrix  $\mathbf{A}$  is

$$a_{ij} = \int_{\Omega} D(\mathbf{r}) \nabla \varphi_i(\mathbf{r}) \cdot \nabla \varphi_j(\mathbf{r}) \, d\mathbf{r} + \int_{\Omega} \mu_a(\mathbf{r}) \varphi_i(\mathbf{r}) \varphi_j(\mathbf{r}) \, d\mathbf{r} + \int_{\partial\Omega} \varphi_i(\mathbf{r}) \varphi_j(\mathbf{r}) / 2\alpha \, d\mathbf{r}, \quad (8)$$

and the component of the matrix  $\mathbf{F}$  is

$$f_{ij} = \varepsilon \int_{\Omega} X(\mathbf{r}) \varphi_i(\mathbf{r}) \varphi_j(\mathbf{r}) \, d\mathbf{r}, \quad (9)$$

where  $\varphi_i$  ( $i = 1, 2, \dots$ ) are the element shape functions. Since the matrix  $\mathbf{A}$  in Eq. (7) is positive definite, we have

$$\Phi = (\mathbf{A}^{-1} \mathbf{F}) \cdot \rho. \quad (10)$$

Because the number of outgoing NIR photons at a surface node is insufficient in general, we prefer integrating detected outgoing photons for a higher signal-to-noise ratio. Hence, from Eq. (10) we obtain the following linear equation for an x-ray pencil beam

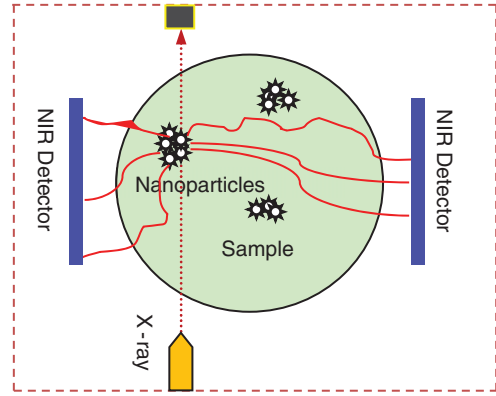


Fig. 2 SXLT system setup that uses x-rays under spectral modulation.

excitation,

$$\sum_{i=1}^n \Phi(\mathbf{r}_{m_i}) = \left( \sum_{m_i} \mathbf{A}^{-1} \mathbf{F} \right) \cdot \rho, \quad (11)$$

where  $m_i$  ( $i = 1, 2, \dots, n$ ) is the index for measurable surface nodes. Note that in the imaging process, the x-ray beam can be moved or modulated multiple times to irradiate the object for a given view, and an array of NIR data will be acquired around the object as shown in Fig. 2. Based on Eq. (11), we can form the linear equation system as follows:

$$Q_e^{-1} \mathbf{M} = \mathbf{G} \cdot \rho, \quad (12)$$

where  $\mathbf{M}$  is the vector from the photon fluence rate data measured with multiple selective excitations,  $Q_e$  is the photon-detector quantum efficiency, and  $\mathbf{G}$  is a weighting matrix assembled with a row vector  $\sum_{m_i} \mathbf{A}^{-1} \mathbf{F}$  for each x-ray excitation. Equation (12) describes the linear relationship between the nanophosphor distribution and the NIR measurement.

### 2.4 Reconstruction

In the CS framework, one can reconstruct a sparse image from far less samples than what the Nyquist sampling theorem demands.<sup>19</sup> Based on the biological characteristics, nanoparticles preferentially seek the specific cells in the tissue, forming a sparse or smooth distribution. As a result, applying an appropriate sparsifying transform  $\mathbf{T}$  (such as the total variation or wavelet transform), the nanophosphor concentration image can be converted into a sparse image that has far fewer significant pixel values than the total number of pixels. Using a CS technique,<sup>19</sup> we can reconstruct a nanoparticle density distribution by solving the following optimization problem

$$\begin{aligned} & \text{minimum } \|\mathbf{T} \cdot \rho\|_1 \\ & \text{subject to } \|\mathbf{G} \cdot \rho - Q_e^{-1} \mathbf{M}\|_2 \leq \tau, \\ & \rho \geq 0 \end{aligned} \quad (13)$$

where  $\tau$  represents the data noise level. The presence of the  $l_1$  term is used to induce the solution sparsity. Equation (13) can be efficiently solved using a contemporary numerical method such as the Bregman iteration.<sup>20</sup>

The above formulation is valid for both single- and multi-spectral x-ray excitation patterns. The induced phosphor luminescent spectra may depend on both the x-ray dose and energy

in a nonlinear fashion, which may or may not be linearly approximated in practical applications. Nevertheless, these details can be readily worked out in a particular scenario if the need arises.

### 3 Numerical Simulation

We performed representative numerical tests to evaluate the proposed SXLCT methodology with a numerical mouse phantom and synthetic measurement data. As shown in Fig. 3, the numerical mouse phantom was established from the CT slices of a mouse using Amira (Amira 4.0, Mercury Computer Systems, Inc., Chelmsford, Massachusetts). The phantom was discretized into 203,690 tetrahedral elements with 58,246 nodes. The emission wavelength of the nanophosphor under x-ray excitation was set to 802 nm, which was based on the emission characteristics of  $Gd_2O_2S$  doped with thulium.<sup>3,4</sup> Based on Ref. 21, the light yield  $\varepsilon$  was assumed to be about  $0.15 \text{ cm}^3/\text{mg}$  for 50 keV.

Appropriate optical parameters were accordingly assigned to the mouse model. The reduced scattering coefficient  $\mu'_s(\lambda)$  relies on the wavelength  $\lambda$  (nm) and is approximated by an empirical function

$$\mu'_s(\lambda) = 10a \cdot \lambda^{-b}, \quad (14)$$

where  $a$  and  $b$  are the constants depending on the tissue type. The parameters  $a$  and  $b$  for organ-specific values can be found.<sup>22</sup> The

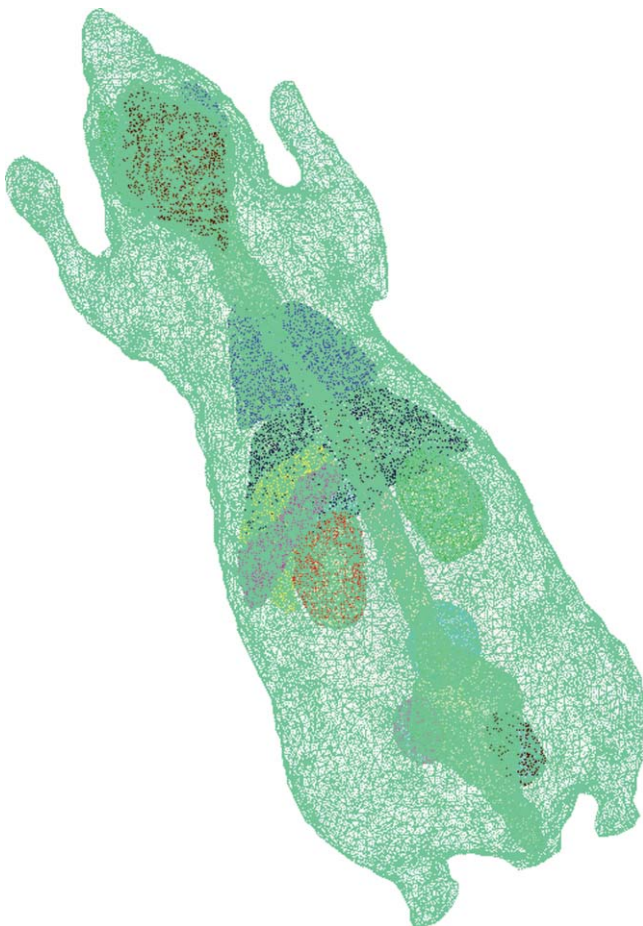


Fig. 3 Mouse phantom represented in a finite element mesh.

tissue absorption depends on the local oxy-hemoglobin ( $HbO_2$ ), deoxy-hemoglobin ( $Hb$ ), and water ( $W$ ) concentrations in the respective organs. The spectral absorption coefficient  $\mu_a(\lambda)$  can be approximated as the weighted sum of the three absorption coefficients  $\mu_{aHbO_2}(\lambda)$ ,  $\mu_{aHb}(\lambda)$ , and  $\mu_{aW}(\lambda)$ , which were calculated from the corresponding absorbance spectra reported in Ref. 22

$$\mu_a(\lambda) = S_B[x\mu_{aHb}(\lambda) + (1-x)\mu_{aHbO_2}(\lambda)] + S_W\mu_{aW}(\lambda), \quad (15)$$

where  $x = HbO_2/(HbO_2 + Hb)$  is the ratio between oxy-hemoglobin and the total hemoglobin concentration,  $S_B$  and  $S_W$  are scaling factors specific to the respective organs.<sup>23</sup> The relative electron density of 0.6 was assigned to the phantom, which corresponds to that of soft tissues.

#### 3.1 Spatial Resolution

Three spherical sub-regions of 0.5 mm diameter were centered at (14.3, 40, 21.8), (12.3, 40, 20.5), and (12.3, 40, 23.0), respectively, and filled with nanophosphor concentrations of  $1.5 \mu\text{g}/\text{mL}$ , to test the spatial resolution. An x-ray source was operated at 50 keV and 30 mA to perpendicularly irradiate the phantom surface at the longitudinal position 40 mm. The x-rays were collimated into a pencil beam of 0.2 mm width. The photon detector quantum efficiency  $Q_E$  was set to 1. The x-ray scattering distribution was calculated based on the x-ray differential scattering cross section and the electron density distribution in the phantom (Fig. 1). The NIR light emitted from the excited nanophosphors underwent scattering and absorption in the phantom, and the intensity of the NIR on the surface of the phantom was simulated according to the DA model. Poisson noise was added to the synthetic measurement data. The image acquisition procedure was repeated 100 times when the x-ray pencil beam was translated in a 0.2 mm increment for a given view. The parallel-beam imaging geometry was rotated 20 times to cover a 360 deg range evenly.

Based on the known geometrical parameters, optical properties, and x-ray energy, we formed Eq. (12) using the finite element method. The linear equation system was quite sparse and efficiently manipulated. In the CS framework, we employed a fast iterative shrinkage-thresholding algorithm (FISTA) (Ref. 20) for the reconstruction of the nanophosphor distribution.

The FISTA optimization algorithm demonstrated an excellent performance in terms of convergence and stability. The reconstructed results are in close agreement with the truth, and the average relative error of the reconstructed nanophosphor density was less than 10%, which was defined as  $\bar{e} = \frac{1}{N} \sum_{k=1}^N \frac{|\Phi_k^S - \Phi_k^T|}{\Phi_k^T}$ , where  $\Phi_k^T$  and  $\Phi_k^S$  are the true and computed nanoparticles concentrations, respectively. Figures 4(a) and 4(c) present the comparison at the cross section through the nanophosphor distribution between the reconstructed and true nanophosphor density distributions.

Then, we repeated the numerical experiment without compensating for x-ray scattering, while the synthetic measurement data on the surface of the phantom were kept intact; that is, which were generated by both the x-ray primary beam and associated x-ray scattering. The results indicated that the reconstructed

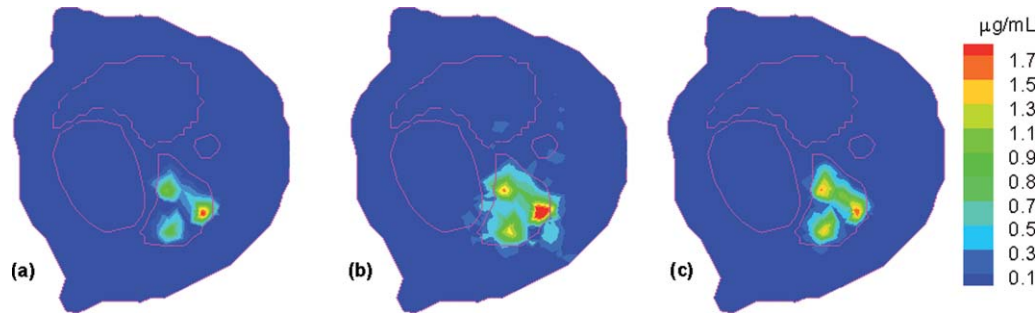


**Fig. 4** Spatial resolution comparison between the reconstructed and true nanophosphor density distributions. (a) Reconstructed nanophosphor density distribution with the proposed SXLCT approach, yielding an average relative error of 10%; (b) reconstructed nanophosphor density distributions assuming no x-ray scattering in the model, yielding an average relative error over 40%; and (c) true nanophosphor density distribution.

average relative error was more than 40% compared to the true nanophosphor density distribution, as shown in Figs. 4(b) and 4(c). In this case, the light source excited by x-ray scattering was mistakenly treated as the luminescence emission due to the x-ray primary beam. Hence, the resultant reconstructed phosphor density distribution was much higher than the truth.

### 3.2 Particle Density Resolution

The detection sensitivity for very low concentrations of probes is significant in molecular and cellular imaging. To evaluate the density resolution of the proposed methodology, the same three spherical sub-regions were assumed in the mouse phantom as above described and filled with the nanophosphor concentrations of  $0.1 \mu\text{g/mL}$ ,  $0.3 \mu\text{g/mL}$ , and  $1.2 \mu\text{g/mL}$ , respectively. The x-ray source of 50 keV and 30 mA was collimated into a pencil beam again to irradiate the phantom at the longitudinal position 40 mm, translated 100 times in a 0.2 mm increment to generate NIR light for a view angle, and rotated 20 times to cover 360 deg for NIR data acquisition.

The reconstruction was similarly conducted as it was previously. Figure 5(a) shows the reconstructed nanophosphor density distributions. The results are also in excellent agreement with the truth in Fig. 5(c). In particular, the results show that our proposed method can identify the phosphor nanoparticles in the concentration level as small as  $0.1 \mu\text{g/mL}$  in the scenario of various nanophosphor densities up to  $1.2 \mu\text{g/mL}$ .

For comparison, we repeated the numerical experiment assuming no x-ray scattering. The measurable photon fluence rate on the surface of the phantom was generated from the lumines-

cence source of nanophosphors excited from the x-ray primary and scattering photons. The results show that the reconstructed nanophosphors density distribution had an average relative error more than 40% relative to the true nanophosphors density distribution, as shown in Figs. 5(b) and 5(c).

### 3.3 Spectrally Resolved Reconstruction

The phosphors can be adapted to emit light signals of different spectra depending on the doping material; for example, Terbium emits green (545 nm) light, and Thulium emits near-infrared (802 nm) light under the 100 keV x-ray irradiation. Different nanophosphors have a variety of fluorescence emission peaks and serve as distinct types of molecular probes for molecular and cellular imaging. In general, the maximum peak emission of a given type of nanophosphors is formed at its x-ray absorption K-edge. Luminescence spectra of different probes can be separated using optical filters and advanced algorithms. For multi-probe optical molecular imaging, we should measure multi-spectral NIR signals on the mouse body surface.

In our numerical simulation, two spherical regions A and B of 0.5 mm diameter were centered at (13.5, 40, 21) and (12.1, 40, 23.0), respectively. The A region was filled with nanophosphors of type A with a concentration of  $0.7 \mu\text{g/mL}$  and nanophosphors of type B with a concentration of  $0.3 \mu\text{g/mL}$ . The B region was filled with nanophosphors of type A with a concentration of  $0.3 \mu\text{g/mL}$  and nanophosphors of type B with a concentration of  $0.7 \mu\text{g/mL}$ . Under the 50 keV x-ray excitation, nanophosphors of type A emit NIR light of 700 nm. Under the 80 keV x-ray

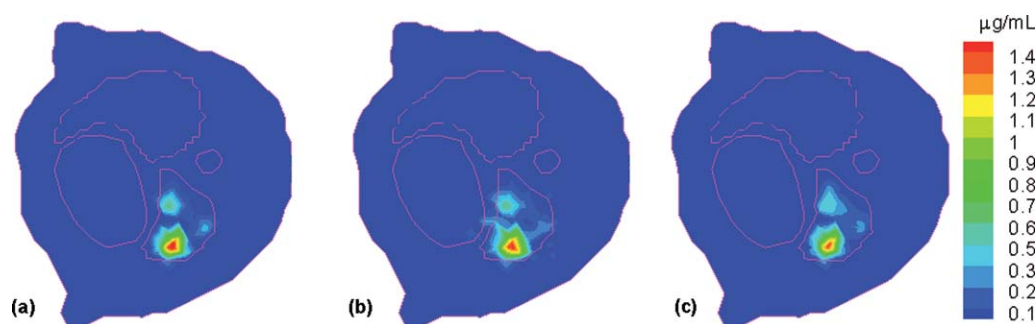


**Fig. 5** Density resolution comparison between the reconstructed and true nanophosphor density distributions. (a) Reconstructed nanophosphor density distribution with the proposed SXLCT approach, producing an average relative error of 12%; (b) reconstructed nanophosphor density distribution assuming no x-ray scattering, resulting in an average relative error over 40%; and (c) true nanophosphor density distribution.

excitation, nanophosphors of type A emit NIR light of 700 nm and nanophosphors of type B emit NIR light of 800 nm. We first excited the numerical phantom with 50 keV x-rays to acquire the NIR signal of 700 nm, and then excited the phantom with 80 keV x-rays to acquire the NIR signals of 700 and 800 nm. In the data acquisition process, the x-ray pencil beam was translated 100 times in a 0.2 mm increment for a given view. The imaging geometry was rotated 20 times to cover a 360 deg range evenly. According to Eq. (12), the linear system equation can be formed to link NIR signals from multiple nanophosphor concentrations in a spectral band  $[\omega_v, \omega_{v+1}]$  to measurable photon fluence rate data in the same spectral band

$$Q_{e,v}^{-1} M_v = \mathbf{G}_v \cdot \rho_v, \quad v = 1, 2, \dots, \kappa, \quad (16)$$

where  $\kappa$  is the number of spectral bands,  $M_v$  consists of measurable photon fluence rate values at the nodes on the object surface in the same spectral band  $[\omega_v, \omega_{v+1}]$ , and  $\rho_v$  is the NIR signals from multiple nanophosphor concentrations in a spectral band  $[\omega_v, \omega_{v+1}]$ , that is,  $\rho_v = \sum_i w_i p_{i,v}$ ,  $v = 1, 2, \dots, \kappa$ , where  $p_{i,v}$  is the  $i$ th probe concentration in a spectral band  $[\omega_v, \omega_{v+1}]$  and  $w_i$  is its weighting factor. Equation (16) can be numerically solved in the compressive sensing framework. Then, we can obtain the individual distributions of a different molecular probes from  $\rho_v$  data using an unmixing technique.<sup>24</sup> Figure 6 shows representative reconstructed images for distributions of probe types A and B, respectively. The reconstructed results are in excellent agreement with the truth.

## 4 Discussions and Conclusion

Let us first compare XFCT and XLCT. On one hand, XFCT and XLCT are similar because both of them can be considered as emission-type tomography with data stimulated

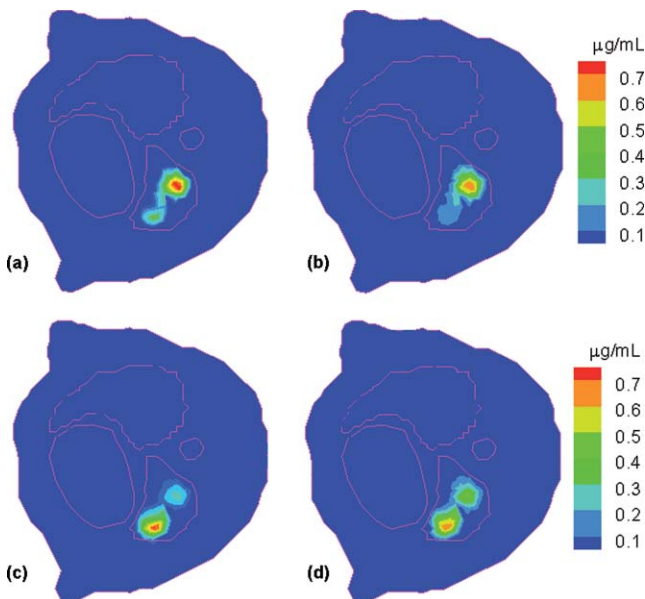


**Fig. 6** Spectral resolution comparison between the reconstructed and true nanophosphor density distributions. (a) Reconstructed distribution for nanophosphors of type A; (b) true distribution for nanophosphors of type A; (c) reconstructed distribution for nanophosphors of type B; and (d) true distribution for nanophosphors of type B.

with external x-rays. On the other hand, there are clear differences between them. Fluorescence refers to photon emission after photon absorption. Luminescence is indirect, such as in the case of nanophosphors. X-rays or gamma rays excite phosphors and other materials via ionization and create luminescence upon recombination of electrons and ions. Most importantly, x-ray fluorescence and luminescence signals are generated with various efficiencies in distinct spectral regions and have different absorption and scattering properties. The former is less strongly absorbed and scattered than the latter.

While the x-ray scattering effect is significant, neither XFCT nor XLCT compensates for such an effect in the image reconstruction process. In the XFCT literature, the scattering effect is treated as noise.<sup>25</sup> In the XLCT work, the Stanford group that developed XLCT has implicitly assumed that the stimulating x-rays traveled strictly in straight lines.<sup>6</sup> To address this source of inaccuracy, the x-ray scattering compensation as we have showcased in this paper must be a key step for either XLCT or XFCT, and especially for the former.

With the rapid development of the x-ray source and detector technology, it is anticipated that in the not-too-distant future x-rays can be cost-effectively delivered wherever (distributed sources), whenever (programmable multiplexing), and whatever (energy modulation) we desire.<sup>26</sup> Therefore, it is valuable and practical to consider various x-ray excitation patterns more complicated than what is currently used for XFCT and XLCT, which is in a pencil beam of a single x-ray spectrum. As suggested above, the spectrally resolving excitation and measurement can be systematically done for optimal image quality, which is especially important for multi-element and/or multi-probe x-ray-excitation-based tomography.

Based on the work on XFCT and XLCT,<sup>6,12</sup> here we have proposed a SXLCT/SXFCT approach to quantify a nanophosphor/element distribution within a biological object. In this initial study, the SXLCT method has been developed to reconstruct a nanophosphor distribution in a small animal model. Upon x-ray excitation, nanophosphors emit NIR light around 700 nm. Within this wavelength range, the NIR light scattering dominates over absorption in the tissue. The photon propagation can be modeled as a diffusive process, and the DA model is quite accurate. The x-ray scattering effect is also important and has been taken into account. Using the finite element method, a linear relationship has been formulated to link the nanophosphor density distribution and the measured NIR data. The CS technique has been applied to solve this inverse problem. The numerical simulation results have demonstrated that the proposed approach can accurately reconstruct the nanophosphor distribution.

There are several topics deserving further research. Since this reconstruction method relies on optical parameters (absorption and scattering coefficients), optical diffuse tomography, photoacoustic tomography, or related techniques should be used to determine such prior knowledge. Also, x-ray scattering tomography techniques should be further developed assuming the availability of spectral x-ray detectors such as MedPix3. Furthermore, XLCT currently works in a pencil beam scanning mode and takes long sampling time. Fan-beam or other scanning modes can improve the imaging efficiency and is under development in our laboratory.

## Acknowledgments

This work was partially supported by the National Institutes of Health Grant Nos. NIH/NHLBI HL098912 and NIH/NCI CA135151.

## References

1. R. F. Minchin and D. J. Martin, "Minireview: nanoparticles for molecular imaging—an overview," *Endocrinology* **151**, 474–481 (2010).
2. X. Qian, X. H. Peng, D. O. Ansari, Q. Yin-Goen, G. Z. Chen, D. M. Shin, L. Yang, A. N. Young, M. D. Wang, and S. Nie, "In vivo tumor targeting and spectroscopic detection with surface-enhanced Raman nanoparticle tags," *Nat. Biotechnol.* **26**, 83–90 (2008).
3. Y. Tian, W.-H. Cao, X.-X. Luo, and Y. Fu, "Preparation and luminescence property of Gd<sub>2</sub>O<sub>2</sub>S:Tb X-ray nano-phosphors using the complex precipitation method," *J. Alloys. Compd.* **433**, 313–317 (2007).
4. M. Xing, W. Cao, T. Pang, X. Ling, and N. Chen, "Preparation and characterization of monodisperse spherical particles of X-ray nanophosphors based on Gd<sub>2</sub>O<sub>2</sub>S:Tb," *Chin. Sci. Bull.* **54**, 2982–2986 (2009).
5. C. Carpenter, G. Pratz, C. Sun, and L. Xing, "Hybrid x-ray/optical luminescence imaging: characterization of experimental conditions," *Med. Phys.* **37**, 4011–4018 (2010).
6. G. Pratz, C. Carpenter, C. Sun, and L. Xing, "X-ray luminescence computed tomography via selective excitation: a feasibility study," *IEEE Trans. Med. Imaging* **29**, 1992–1999 (2010).
7. G. Pratz, C. M. Carpenter, C. Sun, R. P. Rao, and L. Xing, "Tomographic molecular imaging of x-ray-excitable nanoparticles," *Opt. Lett.* **35**, 3345–3347 (2010).
8. Y. Ye, H. Yu, Y. Wei, and G. Wang, "A general local reconstruction approach on a truncated Hilbert transform," *Int. J. Biomed. Imaging* **2007**, 63634 (2007).
9. H. Yu and G. Wang, "Compressive sensing based interior tomography," *Phys. Med. Biol.* **54**, 2791–2805 (2009).
10. J. Yang, H. Yu, M. Jiang, and G. Wang, "High-order total variation minimization for interior tomography," *Inverse Problems* **26**, 035013 (2010).
11. P. Boisseau, "Determination of three dimensional trace element distributions by use of monochromatic x-ray microbeams," PhD Thesis, Massachusetts Institute of Technology (1986).
12. S.-K. Cheong, B. L. Jones, A. K. Siddiqi, F. Liu, N. Manohar, and S. H. Cho, "X-ray fluorescence computed tomography (XFCT) imaging of gold nanoparticle-loaded objects using 110 kVp x-rays," *Phys. Med. Biol.* **55**, 647–662 (2010).
13. J. Als-Nielsen and D. McMorrow, *Elements of Modern X-ray Physics*, Wiley, New York 2001.
14. J. H. Hubbell, W. J. Veigele, E. A. Briggs, R. T. Brown, D. T. Cromer, and R. J. Howerton, "Atomic form factors, incoherent scattering functions, and photon scattering cross sections," *J. Phys. Chem. Ref. Data* **4**, 471–538 (1975).
15. J. Baro, J. Sempau, J. M. Fernandez-Varea, and F. Salvat, "PENELOPE: an algorithm for Monte Carlo simulation of the penetration and energy loss of electrons and positrons in matter," *Nucl. Instrum. Methods Phys. Res. B* **100**, 31–46 (1995).
16. G. Wang, W. Cong, H. Shen, and Y. Zou, "Varying collimation for dark-field extraction," *Int. J. Biomed. Imaging* **2009**, 847537 (2009).
17. J. Welch and M. J. C. van Gemert, *Optical and Thermal Response of Laser-irradiated Tissue*, Plenum, New York (1995).
18. W. Cong, G. Wang, D. Kumar, Y. Liu, M. Jiang, L. Wang, E. Hoffman, G. McLennan, P. McCray, J. Zabner, and A. Cong, "Practical reconstruction method for bioluminescence tomography," *Opt. Express* **13**, 6756–6771 (2005).
19. E. J. Candes, J. Romberg, and T. Tao, "Robust uncertainty principles: exact signal reconstruction from highly incomplete frequency information," *IEEE Trans. Inf. Theory* **52**, 489–509 (2006).
20. A. Beck and M. Teboulle, "A fast iterative shrinkage-thresholding algorithm for linear inverse problems," *SIAM J. Imaging Sci.* **2**, 183–202 (2009).
21. C. W. E. van Eijk, "Inorganic scintillators in medical imaging," *Phys. Med. Biol.* **47**, R85–R106 (2002).
22. G. Alexandrakis, F. R. Rannou, and A. F. Chatzizoiannou, "Tomographic bioluminescence imaging by use of a combined optical-PET (OPET) system: a computer simulation feasibility study," *Phys. Med. Biol.* **50**, 4225–4241 (2005).
23. S. A. Pahl, "Optical properties spectra," Oregon Medical Laser Clinic, <http://omlc.ogi.edu/spectra/index.html> (2001).
24. R. Lansford, G. Bearman, and S. E. Fraser, "Resolution of multiple green fluorescent protein color variants and dyes using two-photon microscopy and imaging spectroscopy," *J. Biomed. Opt.* **6**, 311–318 (2001).
25. E. X. Miquelles and A. R. De Pierr, "Exact analytic reconstruction in x-ray fluorescence CT and approximated versions," *Phys. Med. Biol.* **55**, 1007–1024 (2010).
26. J. Zhang, G. Yang, Y. Cheng, B. Gao, Q. Qiu, Y. Z. Lee, J. P. Lu, and O. Zhou, "Stationary scanning x-ray source based on carbon nanotube field emitters," *Appl. Phys. Lett.* **86**, 184104 (2005).